An Enhanced Nonlinear ADRC Speed Control Method for Electric Propulsion System: Modeling, Analysis, and Validation

Chaoyu Zhang, Chengming Zhang, Liyi Li, *Senior Member, IEEE*, and Hongchen Liu, *Senior Member, IEEE*

***Abstract*—The electric propulsion system is composed of permanent magnet synchronous motor equipped with propeller load. Due to the strong coupling of propeller speed and load torque, they considerably characterize dynamic response and disturbance suppression capabilities of the speed controller. Traditional nonlinear active disturbance rejection control (NADRC) is less effective in dealing with a step change of command speed and large disturbance. In order to provide faster response and stronger disturbance rejection potential, an enhanced NADRC strategy is proposed in this article. Initially, a linear extended state observer is applied to preliminary estimate the total disturbance. Then, using the designed weight regular function, this estimation is introduced into the nonlinear extended state observer with a cascade structure. The convergence, stability, and disturbance estimation performance of the proposed strategy are then analyzed. Finally, experimental validation is performed based on a constructed experimental platform. The results show that the proposed method reasonably enhances the speed response and antidisturbance performances.**

***Index Terms*—Cascaded extended state observer (ESO), electric propulsion system, enhanced nonlinear active disturbance rejection (ENADRC), propeller load.**

I. Introduction

UNDER the requirement of carbon dioxide emission reduction in the aviation industry, solar-powered unmanned aerial vehicles (SPUAV) as new types of UAVs have received increasing attention [1], [2]. High efficiency and light weight of permanent magnet synchronous motors (PMSM) make them applicable in electric propulsion systems to provide the required lift of SPUAVs [3]. On the one hand, the aircraft should be provided by the propeller. In the dynamic adjustment stage, rapid response of propeller is necessary and PMSM needs to bear the torque generated by the propeller. On the other hand, the unsteady incoming flow and other complicated factors lead to the torque ripples generated by the propeller. So, more requirements are necessary for the dynamic response and disturbance suppression of PMSM. Two principal speed control methods are currently popular, namely parameter optimization-based proportional integral and derivative (PID) speed controller and observer-based speed controller.

PID controller is one of the most widely used technologies in industrial applications. However, the PMSM with propeller is strongly nonlinear and coupled. High performance requirements of the system are difficult to be fulfilled by traditional PID speed controller. By development of intelligent algorithms, they are frequently applied in parameter optimization of PID controllers. An improved hybrid particle swarm optimization algorithm was proposed, based on the integral time absolute error (ITAE) as the objective function [4]. Continuous iterative optimization of the PID control parameters gradually reduces the ITAE and enhances the control performance. Experimental results show that this method has good performance in terms of responsiveness and anti-interference characteristics. A dynamic resetting particle swarm algorithm based on Broyden–Fletcher–Goldfarb–Shanno was proposed in [5] to optimize the control parameters. In comparison with the conventional PID control which is susceptible to load perturbations, this online optimization method by parameters can improve system robustness. However, the degree of optimization is limited by the number of fitness calculations. Combination of the swarm learning process algorithm with Q-learning method was used to correct the PID parameters and improve the system performance [6]. Although the above-mentioned methods can enhance system control performance, they inevitably cause long execution time and increase computational complexity.

Using observer to estimate and compensate the uncertainty is another method to improve system control performance. In particular, development of modern control theory provides many schemes for the speed control of PMSM, such as sliding mode [7], [8], backstepping [9], and internal mode [10], [11] controllers. However, due to the large flight height span and complex operating conditions of the solar-powered UAVs, the above-mentioned control method which depends on the model precision is difficult to completely replace the PID speed controller. In order to reduce the dependence on the model accuracy, the idea of active disturbance rejection control (ADRC) was proposed [12]. The main principle is to use the designed

Manuscript received 14 July 2022; revised 29 October 2022; accepted 13 December 2022. Date of publication 29 December 2022; date of current version 14 February 2023. This work was supported by the Research Fund for the National Science Foundation of China under Grant 52122704 and Grant U2141224. Recommended for publication by Associate Editor R. Kennel. *(Corresponding author: Chengming Zhang.)*

The authors are with the School of Electrical Engineering and Automation, Harbin Institute of Technology, Harbin 150001, China (e-mail: 864031457@qq.com; cmzhang@hit.edu.cn; liliyi.hit@gmail.com; fenmiao@hit.edu.cn).

Color versions of one or more figures in this article are available at https://doi.org/10.1109/TPEL.2022.3232323.

Digital Object Identifier 10.1109/TPEL.2022.3232323

extended state observer (ESO) to estimate the total disturbance and compensate it in time in the control law in order to improve the control effect.

ADRC can be classified as linear structure (LADRC) and nonlinear structure (NADRC) according to different choices of control gain. The control gain of LADRC is fixed, and implementation of the bandwidth method for parameter tuning is simple [13]. At the same time, the control effect is not characterized by variation of disturbance amplitude, which limits its convergence speed under small disturbances. NADRC uses a nonlinear function instead of the fixed gain, which makes the control more flexible, though it increases the complexity of parameter adjustment. The effect of multiple parameter variations on control performance of the system was compared and analyzed in [14]. Because of the time-varying nature of its control gain, the control effect was better when the disturbance changed more slowly. For large disturbance amplitude, due to its small gain under large error, its disturbance observation ability is seriously reduced, which means response speed is slower. Therefore, the ability of NADRC to suppress large-scale disturbances is limited [15].

Cascade ESO is a suitable choice to improve the control performance of ADRC. A cascaded ESO design was conducted in [16] and [17] for disturbance estimation of PMSM system, which significantly improved the antidisturbance potential of the system. Unfortunately, the above-mentioned experiments were carried out on the motor test platform such that the speed and torque of the tested motor were decoupled. In the electric propulsion system, because of the coupling characteristics of the propeller, the load torque generated by the propeller changes with the motor speed. This means that better performance of disturbance estimation is required when the command speed after a step change.

This article proposes an enhanced NADRC speed control method based on the conventional NADRC in order to study the applicability of cascaded ESO to PMSM system coupled with propeller load. The method first utilizes linear extended state observer (LESO) for initial estimation of system disturbance. The resulted estimate is then introduced into nonlinear extended state observer (NESO) according to the designed weight rule function in order to improve the performance of NESO. The rest of this article is organized as follows. Section II describes the mathematical model of PMSM and propeller. The design guidelines of the enhanced NADRC are introduced in Section III, and its characterization is analyzed in Section IV. The coupling system is implemented to carry out experiments, and effectiveness of the proposed algorithm is verified based on speed step response and disturbance simulation in Section V. Finally, Section VI concludes this article.

II. System Mathematical Model

A. Mathematical Model of PMSM

The voltage equivalent equations of PMSM in the *dq*-axis are expressed as follows [18]:

$$\frac{di_d}{dt} = -\frac{R_s}{L_d}i_d + \frac{1}{L_d}u_d + \frac{L_q}{L_d}\omega_e i_q$$

$$\frac{di_q}{dt} = -\frac{R_s}{L_q}i_q + \frac{1}{L_q}u_q - \frac{\omega_e}{L_q}(L_d i_d + \Psi_f) \tag{1}$$

where R_s, L_d, and L_q are the phase resistance, and two direct quadrature inductances, respectively. Ψ_f is the permanent magnetic flux linkage, ω_e is the electrical velocity, u_d and u_q indicate the voltages, and i_d and i_q denote the currents in the *dq*-axis. For the surface-mounted PMSM (SPMSM), $L_d = L_q$. Neglecting the viscosity coefficient, the torque and the mechanical equations of PMSM are given as follows:

$$T_e = \frac{3}{2}p\Psi_f i_q \tag{2}$$

$$\begin{cases} \frac{d\omega_r}{dt} = \frac{1}{J}T_e - \frac{T_L}{J} = bi_q^* + f \\ f = \frac{3p}{2J}\Psi_f\left(i_q - i_q^*\right) - \frac{T_L}{J} \end{cases} \tag{3}$$

where ω_r is the actual speed of PMSM, T_e is the electromagnetic torque, and T_L is the load torque under the propeller action. J denotes the moment of inertia and p is the number of pole pairs, such that $\omega_r = \omega_e/p$. i_q^* is the *q*-axis current command, b is the torque current gain, and $b = 3p\Psi_f/2J$. The sum of internal and external total disturbances to the system is notified by f.

B. Propeller Characteristics

The thrust demand of SPUAV must be supplied by propeller. Due to aerodynamic effects [19], [20], the propeller provides the required thrust while its torque must be supplied by PMSM. The torque(T_L) and thrust(F) generated by the propeller can be expressed as follows:

$$\begin{aligned} T_L &= C_T\rho\omega_r^2 D_p^5 \\ F &= C_F\rho\omega_r^2 D_p^4 \end{aligned} \tag{4}$$

where ρ is the air density and D_p represents the propeller radius. C_T and C_F denote the torque and thrust coefficients, respectively, which are nonlinear real variable functions of relative inflow velocity, Reynolds number, and Mach number.

From (4), it can be seen that the propeller acts on the PMSM. Accordingly, the torque and speed are strongly coupled, and the speed regulation performance affects the load current.

III. Enhanced Nonlinear ADRC Speed Controller Design

The above-mentioned discussion about LADRC and NADRC indicates that both of them have certain limitations under different disturbance forms. Therefore, the cascade form of linear and nonlinear ESOs can be used to replace the traditional nonlinear ESO. Fig. 1(a) describes that the speed and current double closed loop system is used to control SPMSM, in which the speed loop uses the enhanced NADRC algorithm and the current loop uses the PI algorithm. Fig. 1(b) details the specific structure of the enhanced NADRC.

A. Cascade Extended State Observer

1) Linear Extended State Observer: First, a LESO with fixed gain characteristics is used to preliminarily estimate the total

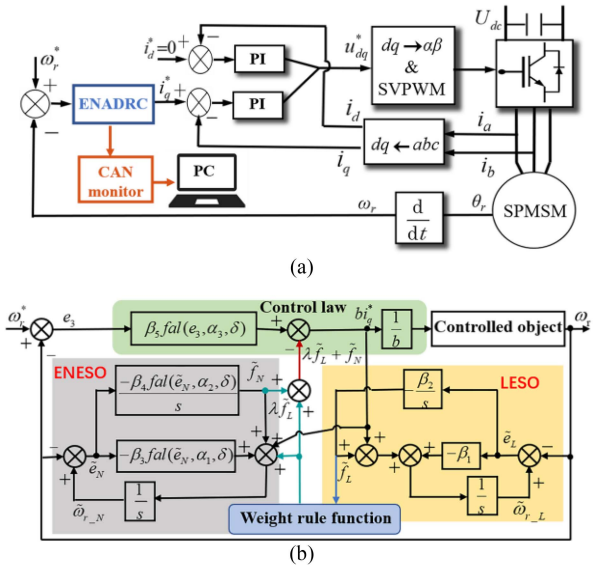

Fig. 1. Block diagram of enhanced NADRC structure for an SPMSM driver. (a) Enhanced NADRC speed control system for SPMSM. (b) Detailed structure of enhanced NADRC.

system disturbance, which is expressed as follows:

$$\begin{cases} \tilde{e}_L = \tilde{\omega}_{r\_L} - \omega_r \\ \dot{\tilde{\omega}}_{r\_L} = bi_q^* + \tilde{f}_L - \beta_1 \tilde{e}_L \\ \dot{\tilde{f}}_L = -\beta_2 \tilde{e}_L \end{cases} \tag{5}$$

where ω_r and $\tilde{\omega}_{r\_L}$ represent the actual and observed values of propeller speed, respectively. $\tilde{f}_L$ is the observed result of the disturbance, and β_1 and β_2 are the gain parameters of LESO. $\tilde{e}_L$ represents the error between $\tilde{\omega}_{r\_L}$ and ω_r.

2) Enhanced Nonlinear Extended State Observer (ENESO): By introducing the initial estimate of LESO for the disturbance as a known part into the NESO, the following state equation can be established:

$$\begin{cases} \tilde{e}_N = \tilde{\omega}_{r\_N} - \omega_{\mathrm{r}} \\ \dot{\tilde{\omega}}_{r\_N} = bi_q^* + \tilde{f}_N + \lambda \tilde{f}_L - \beta_3 fal\left(\tilde{e}_N, \alpha_1, \delta\right) \\ \dot{\tilde{f}}_N = -\beta_4 fal\left(\tilde{e}_N, \alpha_2, \delta\right) \end{cases} \tag{6}$$

where $\tilde{\omega}_{r\_N}$ is the propeller speed observation obtained by the nonlinear function, $\tilde{e}_N$ is the error between observed and actual speeds, and $\tilde{f}_N$ is the disturbance observation result except for $\lambda \tilde{f}_L$. α_1, α_2 and δ are the parameters of the nonlinear function, and β_3 and β_4 are the gain parameters of NESO. λ is the defined weighted rule function. Notably, this ESO is equivalent to the traditional NESO if $\lambda = 0$.

3) Characteristics of Nonlinear Function fal*(e, α_i, δ):* *fal*(*e*, α_i, δ) is a function with nonlinear characteristics, which is defined as follows [20]:

$$fal\left(e, \alpha_i, \delta\right) = \begin{cases} |e|^{\alpha_i} \operatorname{sign}\left(e\right), |e| > \delta \\ e / \delta^{1-\alpha_i}, |e| \le \delta \end{cases} \tag{7}$$

where α_i is a nonlinear factor determining the shape of nonlinear function, δ characterizes the size of nonlinear interval, sign (•) denotes a sign function. The function features in (3) are represented in Fig. 2. According to different choices of proportional,

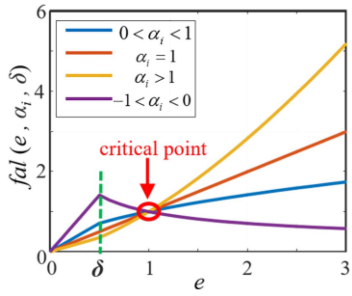

Fig. 2. Function characteristic curve of *fal*(*e*, α_i, δ) [21].

integral, and differential modes, the value of α_i can affect the system performance, and it is characterized as follows:

a) *Proportional mode:* A large value of *fal*(*e*, α_i, δ) is expected when error is small, in order to improve tracking performance. Conversely, when the error is large, a small value of *fal*(*e*, α_i, δ) is desired to reduce the impact. In this mode, considering α in the range of $0 < \alpha_i < 1$ is more appropriate for *fal*(*e*, α_i, δ).

b) *Integral mode:* In this mode, the range of $-1 < \alpha_i < 0$ is more suitable for *fal*(*e*, α_i, δ). When the error is small, *fal*(*e*, α_i, δ) increases and the integration effect will dominate. In contrast, when the error is larger, *fal*(*e*, α_i, δ) gradually decreases, which can effectively avoid the saturation phenomenon of the integration link.

c) *Differential mode:* In this case, $\alpha_i > 1$ is appropriate for *fal*(*e*, α_i, δ). By this range, *fal*(*e*, α, δ) decreases for smaller errors, while it increases when the error is large. This diminishes the differential effect around the target value.

It is worth noting that when $\alpha = 1$, *fal*(*e*, α_i, δ) will be a linear feature, which is a special case. At the same time, when $e = 1$ is a critical point, any value of α_i in this state has no effect on *fal*(*e*, α_i, δ). For the propulsion system, the value of α_i is more suitable for proportional mode. δ brings discontinuity, and the effect of its value is analyzed in the next section.

4) α_i and δ Parameters Selection: Equivalent gain method can be used for (7), and its expression is as follows:

$$\frac{fal\left(e, \alpha_i, \delta\right)}{e} \times e = \tau_i\left(e\right) \times e. \tag{8}$$

According to the above-mentioned equation, *fal*(*e*,α_i ,δ) can be equated to the product of e and $\tau_i(e)$.$\tau_i(e)$ is the nonlinear gain of the error correlation. Clearly, the values of α_i and δ have an important impact on $\tau_i(e)$. The results are shown in Fig. 3.

As can be seen from Fig. 3(a), when α_i is fixed, the constant value interval of $\tau_i(e)$ increases with the growth of δ. Therefore, it is necessary to determine a suitable constant value interval. Generally, it is better to take the value of $0.02 < \delta < 0.1$. According to Fig. 3(b), the gain of $\tau_i(e)$ increases with the decrease of α_i when $|e| \le 1$. This situation is reversed for $|e| > 1$. However, if α_i value is too small, it may cause high frequency tremor. If α_i value is too large, it cannot play the advantages of fast error attenuation and strong antidisturbance ability. According to experience, $\alpha_1 > \alpha_2$ is generally appropriate.

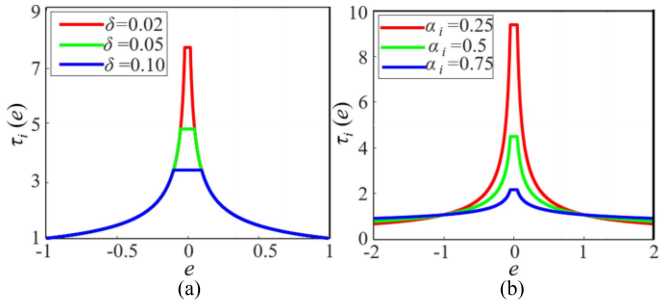

Fig. 3. Comparison of $\tau_i(e)$ curve. (a) Different δ with $\alpha_i = 0.5$. (b) Different α_i with $\delta = 0.05$.

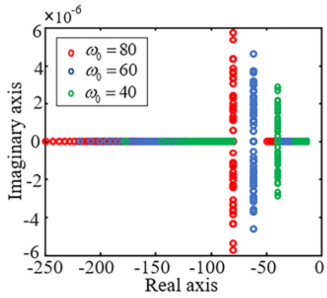

Fig. 4. Variation of characteristic roots with $\tilde{e}_N$.

B. Control Law Design

The disturbance synthesis observations $\lambda\tilde{f}_L$ and $\tilde{f}_N$ of the cascaded ESO are used to design the current command control law, as presented in (5)

$$\begin{cases} e_3 = \omega_r^* - \omega_r \\ i_q^* = \dfrac{\beta_5 fal(e_3,\alpha_3,\delta) - \left(\lambda\tilde{f}_L + \tilde{f}_N\right)}{b} \end{cases} \tag{9}$$

where β_5 is the proportional coefficient and $e_3$is the error between ω_r^* and ω_r.

C. Function Rule Design for the Weight Value λ

Since $fal(e_3, \alpha_3, \delta)$ is used in the control law, so the value of λ can be increased after a step change in the speed command. This approach enhances the ability to estimate the total disturbance by $\lambda\tilde{f}_L$. Then, λ can be appropriately reduced around the target speed in order to enhance the proportion of $\tilde{f}_N$ in the total disturbance estimation. Specifically, the following function design is adopted to adjust the weight value λ:

$$\lambda = \begin{cases} \lambda_{\max}, |e_3| \geq e_2 \\ \lambda_{\min} + (\lambda_{\max} - \lambda_{\min}) \dfrac{|e_3| - e_1}{e_2 - e_1}, e_1 < |e_3| < e_2 \\ \lambda_{\min}, |e_3| \leq e_1 \end{cases} \tag{10}$$

where $\lambda_{\max}$ and $\lambda_{\min}$ are the upper and lower limits of the weight coefficients, e_1 and e_2 are the upper and lower bounds of the selected error, respectively.

IV. Characteristic Analysis of ENADRC

A. Convergence of ENESO

According to equations (8), ENESO can be regarded as a LESO with variable gain structure. Then, the estimation error of total disturbance is $\tilde{e}_f = \tilde{f}_N + \lambda\tilde{f}_L - f$. After Laplace transform and sorting, the expressions of errors can be obtained as follows:

$$\tilde{e}_N(s) = \frac{(\lambda\beta_2 B - A)\, s}{A \times B}\left[s\omega_r(s) - bi_q^*(s)\right] \tag{11}$$

$$\tilde{e}_f(s) = \frac{(\lambda\beta_2 B - A) \times \beta_4\tau_2(\tilde{e}_N) - \lambda\beta_2 B}{A \times B}\left[bi_q^*(s) - s\omega_r(s)\right] \tag{12}$$

where $\tilde{e}_N(s)$and $\tilde{e}_f(s)$ are Laplace transforms of $\tilde{e}_N$ and $\tilde{e}_f$, respectively. Furthermore, $\omega_r(s)$ and $i_q^*(s)$ are Laplace transforms of ω_r and i_q^*, respectively. $A = s^2 + \beta_1 s + \beta_2$ and $B = s^2 + \beta_3\tau_1(\tilde{e}_N)s + \beta_4\tau_2(\tilde{e}_N)$. s is the Laplace operator.

It is obvious that the transfer function of each error has the same characteristic equation

$$A \times B = \left(s^2 + \beta_1 s + \beta_2\right) \times \left[s^2 + \beta_3\tau_1\left(\tilde{e}_N\right)s + \beta_4\tau_2\left(\tilde{e}_N\right)\right]. \tag{13}$$

There are many parameters to be determined in (13). For *A*, introducing bandwidth ω_o to simplify the design of β_1 and β_2 is a common method in [13]. When $\beta_1 = 2\omega_o$ and $\beta_2 = \omega_o^2$, *A* is equivalent to $(s + \omega_o)^2$. For *B*, we can also use this concept, but $\tau_i(\tilde{e}_N)$ is variable, excessive β_4 may cause overshoot oscillation of disturbance estimation in [14]. Therefore, the value of β_4 can be appropriately reduced. $\beta_3 = 2\omega_o$ and $\beta_4 = \omega_o^2/2$ can be determined. In this way, the four control parameters in *A* and *B* can be changed by adjusting ω_o, which simplifies the complex parameter adjustment process.

Since $\tau_i(\tilde{e}_N)$ is changing with $\tilde{e}_N$, the characteristic roots of the above-mentioned equation are also varying. Therefore, it is necessary to make the trajectory of the characteristic roots moving in the *s*-plane with $\tilde{e}_N$, and the result is shown in Fig. 4.

As can be seen from Fig. 4, the characteristic roots are always located in the left half of the *s*-plane when $\tilde{e}_N$ varies, i.e., for any $\tilde{e}_N$, the system gradually converges to the equilibrium state, so ENESO has good convergence. Intuitively, the reduction of ω_0 causes the characteristic roots to move to the right.

B. Nonlinear fal(e, α_i, δ) Based on Describing Function

As can be seen from Fig. 1(b), the system contains three nonlinear links, which cannot be directly analyzed in frequency domain. Describing function is an effective method to extend the frequency response method in linear system to nonlinear system. Especially in the field of stability analysis of nonlinear system, describing function plays a great role.

According to [20] and [22], if the input error $e(t)$ is $E\sin\omega t$, the actual output can be approximated by fundamental component of the nonlinear link output. The result of fundamental component is expressed as follows:

$$B_i(E) = \begin{cases} \frac{E}{\delta^{1-\alpha_i}}, E \leq \delta \\ \frac{4}{\pi}\left[\int_0^{\gamma} \frac{E}{\delta^{1-\alpha_i}}\sin^2\omega t d\omega t + \int_{\gamma}^{\frac{\pi}{2}} E^{\alpha_i}(\sin\omega t)^{1+\alpha_i} d\omega t\right], E > \delta \end{cases} \tag{14}$$

where E and ω are the amplitude and frequency of the input error. $\gamma = \arcsin(\delta/E)$. When α_i is not an integer, it is difficult to express the integral result from γ to $\pi/2$. Therefore, the area of

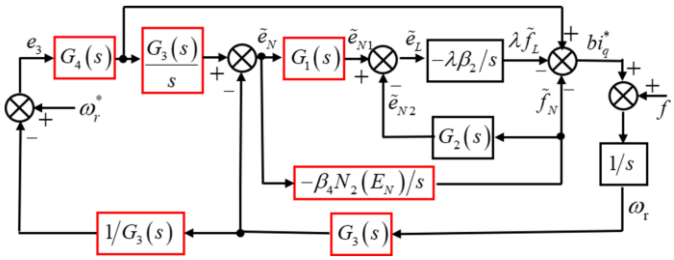

Fig. 5. Equivalent control block diagram of enhanced NADRC. Red boxes represent transfer functions with nonlinear characteristics.

the integrated function on the interval can be used to approximate the result. Define describing function $N_i(E) = B_i(E)/E$, then $N_i(E)$ for $\alpha_1 = 0.75$, $\alpha_2 = 0.5$ and $\delta = 0.05$ can be expressed as follows:

$$N_1(E) = \begin{cases} \frac{1}{\delta^{0.25}}, E \le \delta \\ \frac{2}{\pi\delta^{0.25}}\left(\gamma - \frac{\delta}{E}\sqrt{1-\left(\frac{\delta}{E}\right)^2}\right) \\ +\frac{4}{\pi\delta^{0.25}}\begin{bmatrix}\left(\frac{\pi}{2}-\gamma\right) - a_1 \times \left(\frac{\pi}{2}-\gamma\right)^3 \\ +b_1 \times \left(\frac{\pi}{2}-\gamma\right)^5\end{bmatrix}, E > \delta \end{cases} \tag{15}$$

$$N_2(E) = \begin{cases} \frac{1}{\delta^{0.5}}, E \le \delta \\ \frac{2}{\pi\delta^{0.5}}\left(\gamma - \frac{\delta}{E}\sqrt{1-\left(\frac{\delta}{E}\right)^2}\right) \\ +\frac{4}{\pi\delta^{0.5}}\begin{bmatrix}\left(\frac{\pi}{2}-\gamma\right) - a_2 \times \left(\frac{\pi}{2}-\gamma\right)^3 \\ +b_2 \times \left(\frac{\pi}{2}-\gamma\right)^5\end{bmatrix}, E > \delta \end{cases} \tag{16}$$

where $a_1 = 0.2772$ and $b_1 = 0.03546$ are fitting coefficients of $\alpha_1 = 0.75$. Similarly,$a_2 = 0.2408$ and $b_2 = 0.02552$ are fitting coefficients of $\alpha_2 = 0.5$.

C. Stability Analysis Based on Harmonic Balance Method

Fig. 1(b) can be equivalent by using describing function, as shown in Fig. 5. Essentially, $N_i(E)$ affects the amplitude of the output result. The equivalent transfer function is shown in the following equation:

$$\begin{cases} G_1(s) = \frac{s^2+\beta_3 N_1(E_N)s}{s^2+\beta_1 s+(1-\lambda)\beta_2}, G_3(s) = \frac{s}{s+\beta_3 N_1(E_N)} \\ G_2(s) = \frac{s}{s^2+\beta_1 s+(1-\lambda)\beta_2}, G_4(s) = \beta_5 N_3(E_3) \end{cases}. \tag{17}$$

Actually, each transfer function is an adjustment of the amplitude and phase of the input signal. Assuming $\tilde{e}_N = E_N \sin\omega t$, the main parts of the system can be expressed as follows:

$$\begin{cases} \tilde{f}_N = E_{f_N}\cos\omega t, \tilde{e}_{N1} = E_{N1}\sin(\omega t+\varphi_1) \\ \tilde{e}_{N2} = E_{N2}\cos(\omega t+\varphi_2), \tilde{e}_L = E_L\sin(\omega t+\varphi_L) \\ \lambda\tilde{f}_L = \lambda\beta_2 E_L\cos(\omega t+\varphi_L), \lambda\tilde{f}_L+\tilde{f}_N = M\sin(\omega t+\varphi_M) \end{cases} \tag{18}$$

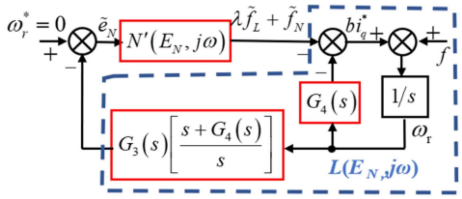

Fig. 6. Simplified control block diagram based on Fig. 5.

$$\begin{cases} E_{f_N} = \beta_4 N_2(E_N)/\omega \\ E_{N1} = E_N\sqrt{C_1^2+D_1^2}, \varphi_1 = \arctan(D_1/C_1) \\ E_{N2} = E_{f_N}\sqrt{C_2^2+D_2^2}, \varphi_2 = \arctan(D_2/C_2) \\ G = E_{N1}\cos\varphi_1 + E_{N2}\sin\varphi_2, H = E_{N1}\sin\varphi_1 - E_{N2}\cos\varphi_2 \\ E_L = \sqrt{G^2+H^2}, \varphi_L = \arctan(H/G) \\ I = \lambda\beta_2 E_L\cos\varphi_L/\omega + E_{f_N}, K = -\lambda\beta_2 E_L\sin\varphi_L/\omega \\ M = \sqrt{I^2+K^2}, \varphi_M = \arctan(I/K) \end{cases} \tag{19}$$

where E_{f_N}, E_{N1}, E_{N2}, E_L, and M are the amplitudes of corresponding parts. C_1 and D_1 are the real and imaginary parts of $G_1(s)$. C_2 and D_2 are the real and imaginary parts of $G_2(s)$. φ_1 and φ_2 are the phase changes corresponding to $G_1(s)$ and $G_2(s)$. G and H are the expressions after sorting by $\tilde{e}_{N1} - \tilde{e}_{N2}$. Similarly, I and K are the expressions after sorting according to $\lambda\tilde{f}_L + \tilde{f}_N$. φ_L and φ_M are the adjusted phases.

Furthermore, the equivalent transfer function of $\tilde{e}_N$ and $\lambda\tilde{f}_L + \tilde{f}_N$ can be expressed as follows:

$$N'(E_N, j\omega) = \frac{M}{E_N}e^{j\varphi_M}. \tag{20}$$

Based on the above-mentioned results, Fig. 5 can be further simplified to and analyzed based on harmonic balance method. Since the harmonic balance method focuses more on the stability of nonlinear structure, rather than the detailed study of the response and internal state under different inputs. Here, we make $\omega_r^* = 0$ and simplify the system without changing the law of signal transfer function, as in Fig. 6.

Assuming the total disturbance $f = 0$ in Fig. 6, the content in the blue dotted bordered can be equivalent to

$$L(E_N, j\omega) = -G_3(s)\left[\frac{s+G_4(s)}{s}\right] \times \frac{1}{s+G_4(s)}. \tag{21}$$

The characteristic equation of the above quasi-linearized system can be expressed as follows:

$$1 + N'(E_N, j\omega) \times L(E_N, j\omega) = 0. \tag{22}$$

The system stability can be determined using the relationship between $N'(E_N, j\omega) \times L(E_N, j\omega)$ and point $(-1, j0)$. Setting $\omega_o = 60$, $\alpha_1 = 0.75$, $\alpha_2 = 0.5$, $\delta = 0.05$ and $\lambda = 0.5$, the curves in the s-plane are shown in Fig. 7.

Under different E_N in Fig. 7, the curves neither circle nor cross point $(-1, j0)$, so the enhanced nonlinear active disturbance rejection (ENADRC) system is stable. To further analyze λ, Fig. 8 shows the influence of λ with different values on the curves. When E_N is equal to 0.05, the growth of λ makes the curves gradually close to point $(-1, j0)$, although all these curves are satisfied with stability. Similarly, the results are shown in $E_N = 10$. However, it is worth noting that when λ is equal to 0.8, a nonsmooth change in the curve as $\omega \to \infty$.

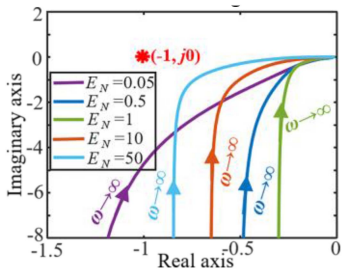

Fig. 7. Stability results under different E_N.

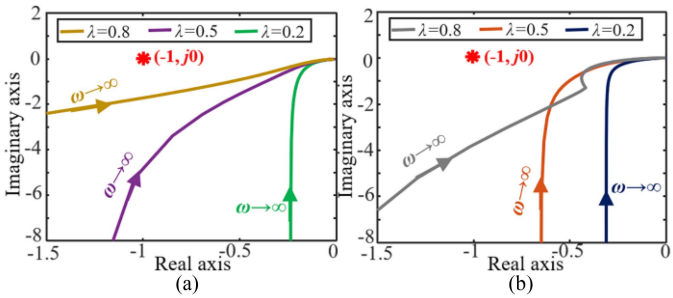

Fig. 8. Effect of different λ on the curves. (a) $E_N = 0.05$. (b) $E_N = 10$.

D. Performance Analysis of $\lambda\tilde{f}_L + \tilde{f}_N$

Since $\lambda\tilde{f}_L + \tilde{f}_N$ serves as an estimate of the total disturbance, the value of λ is very important to the disturbance estimation performance. According to Fig. 6 and (3), the frequency characteristic of f can be expressed as follows [23]:

$$f = s\omega_r - bi_q^* = F\sin(\omega t + \varphi_F) \tag{23}$$

$$\begin{cases} N = E_N\sqrt{\omega^2 + [\beta_3 N_1(E_N)]^2}, \varphi_N = \arcsin(\omega/N) \\ F = \sqrt{N^2 + M^2 - 2MN\cos(\varphi_M - \varphi_N)} \\ \varphi_F = \arctan\frac{M\sin\varphi_M - F\sin\varphi_N}{M\cos\varphi_M - F\cos\varphi_N} \end{cases} \tag{24}$$

where N and F represent the amplitudes of corresponding parts. φ_N and φ_F represent the phase changes.

Using (18) and (23), the evaluation transfer function between them can be established

$$G(E_N, j\omega) = \frac{\lambda\tilde{f}_N + \tilde{f}_L}{f} = \frac{M\sin(\omega t + \varphi_M)}{F\sin(\omega t + \varphi_F)} = \frac{M}{F}e^{j(\varphi_M - \varphi_F)}. \tag{25}$$

In particular, $\tilde{\omega}_{r\_N}$ does not contain $\tilde{f}_L$ when $\lambda = 0$, which means that ENESO is a traditional NESO. Fig. 9 examines disturbance evaluation results for different values of λ under a wide range of E_N. As E_N increases substantially, the estimation performance of traditional ESO for f decreases significantly. The introduction of λ makes this attenuation well-improved. With the increase of λ, the improvement effect is more significant. For large disturbance variations, this implies that ENESO has good estimation performance, which is conducive to improving the antidisturbance potential of the system.

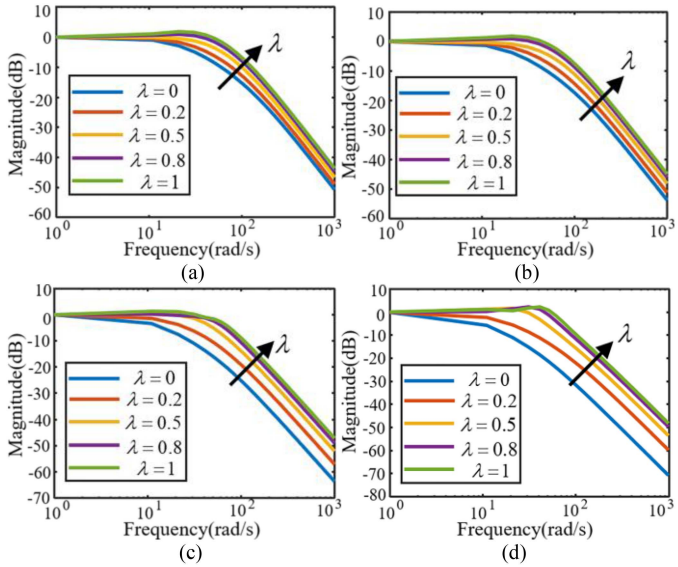

Fig. 9. Results of disturbance evaluation with different λ. (a) $E_N = 0.5$. (b) $E_N = 1$. (c) $E_N = 10$. (d) $E_N = 50$.

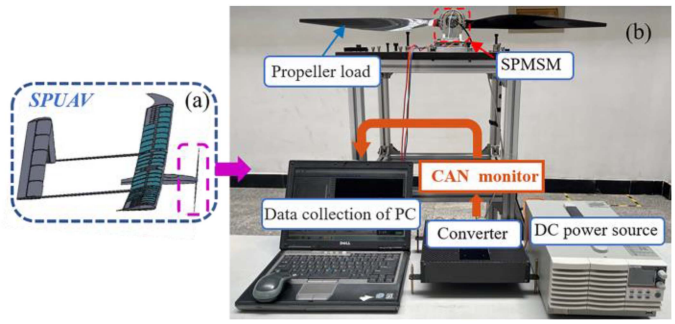

Fig. 10. Electric propulsion system experimental platform. (a) System application model. (b) Laboratory simulation of electric propulsion system.

TABLE I
PARAMETERS OF SYSTEM

	Parameters	Value	Parameters	Value
SPMSM	Rated power	167 W	Stator inductance	420 μH
	Bus voltage	100 V	Rated speed	1000 rpm
	Pole numbers	10	Rated torque	1.59 Nm
	Stator resistance	0.335 Ω	Torque coefficient	0.57 Nm/A
Propeller	Diameter	1.4 m	Rotary inertia	0.035 kg•m^2
	Weight	250 g	Air density	1.225 kg/m^3

V. Experimental Results

According to the above-mentioned description, the system experimental platform consisting of SPMSM and propeller load is built as shown in Fig. 10. The switching frequency of the driver is set to 10 kHz, and the system parameters are presented in Table I. The drive control parameters are selected as $\omega_o = 60$, $\alpha_1 = 0.75$, $\alpha_2 = 0.5$, $\delta = 0.05$, $b = 15$, and $\beta_5 = 30$. The experimental results are captured via CAN protocol connected with the converter.

The first step of experiment is to compare the effect of different values of λ on the speed regulation performance of the step speed command. In the second step, λ is dynamically adjusted in the range of $\lambda_{\min}$ and $\lambda_{\max}$ using the designed weight rule function,

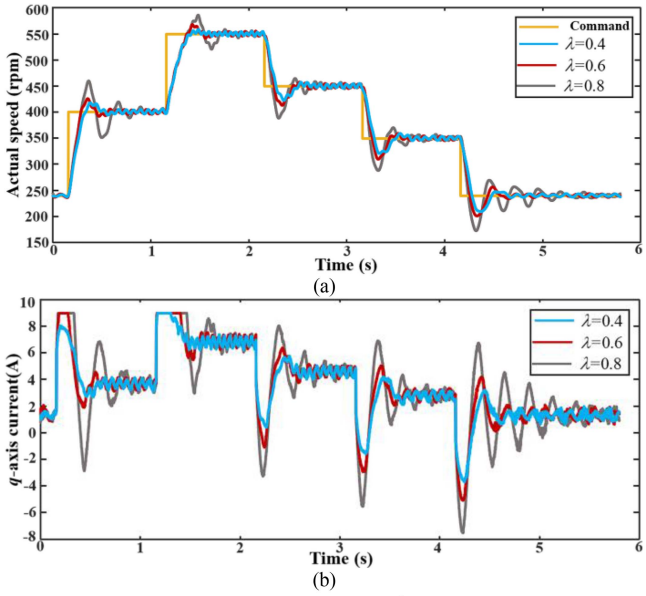

Fig. 11. Response curves for different values of λ. (a) Speed step response. (b) q-axis current response.

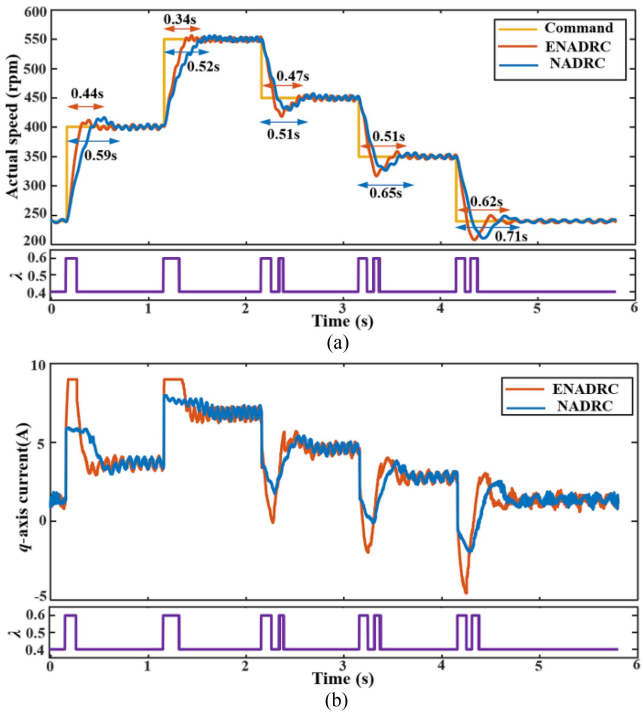

Fig. 12. Comparison of the response curves of NADRC and ENADRC in terms of (a) speed step response and (b) q-axis current response.

and it is then compared with the conventional NADRC. Finally, the impact of simulated disturbances on the two mentioned control strategies is analyzed.

A. Speed Regulation Experiment With Fixed λ

In order to evaluate the response of λ to the step command, the experiment is conducted based on different values of $\lambda = 0.4$, $\lambda = 0.6$ and $\lambda = 0.8$. The speed command change process is as follows: the initial speed is 240 rpm with the steady-state torque of 0.48 Nm; after 0.16 s, the speed command is changed to 400 rpm for 1 s with the steady-state torque of 1.6 Nm; subsequently, the speed command is increased to 550 rpm for 1 s with the steady-state torque of 3 Nm; at 2.16 s, the speed command is reduced to 450 rpm for 1 s with the steady-state torque of 2 Nm; Then, the speed is further reduced to 350 rpm for 1 s with the steady-state torque of 1 Nm; eventually, the speed is restored to 240 rpm and it is maintained constant for 1.64 s. In this way, the experimental cycle is completed by the overall cycle period of 5.8 s. The experimental results are illustrated in Fig. 11.

It can be seen from experimental results that growth of λ significantly increases the overshoot of the system response speed at the command step change. At the same time, the growth of λ increases the time for q-axis current to maintain the maximum current limit during the speed-up region, and the q-axis current changes more violently during the speed-down region. Therefore, the selected limits in this article are $\lambda_{\max} = 0.6$ and $\lambda_{\min} = 0.4$.

B. Speed Regulation Experiment With Adjustable λ

According to experimental results of speed regulation for fixed values of λ in the previous section, the limits of $\lambda_{\min}$ and $\lambda_{\max}$ were determined for the respective values of e_1 and e_2, and the speeds 15 and 30 rpm were selected for the experiment.

Fig. 12(a) compares the response of NADRC and ENADRC to the step command speed. From the results, ENADRC has faster speed response and shorter steady-state time compared with NARDC. However, the overshoot of ENADRC is slightly greater than that of NADRC in the speed-down region. In terms of q-axis current in Fig. 12(b), NADRC does not reach the maximum current limit during the speed-up region compared with ENADRC. This means that ENADRC makes the actual speed of propeller rise faster. Also, as the actual speed approaches the command speed, the reduction of λ is beneficial to suppress the speed overshoot.

C. Comparison of Disturbance Simulation Experiment

In the actual working environment of electric propulsion system, the disturbance of wind will cause the fluctuation of the speed and torque with the propulsion motor. However, such situation is difficult to simulate in the traditional motor test platform. Therefore, referring to the method in [24] and [25], a component is super-imposed on the control law output to simulate disturbance. In order to investigate the influence of disturbance changes on the system tracking performance, the disturbance simulation is carried out at 450 rpm and 550 rpm, with the nondisturbance steady-state torques of 2 Nm and 3 Nm, respectively. In this section, different step torque current commands are added to simulate the impact of disturbance changes on NADRC and ENADRC speed control. First, the target speed is set. After stabilization of the actual speed, additional i_q^* is applied to simulate the increase of torque tracking error caused by the reduction of load torque. Here, the maximum load torque generated by the propeller is mainly considered,

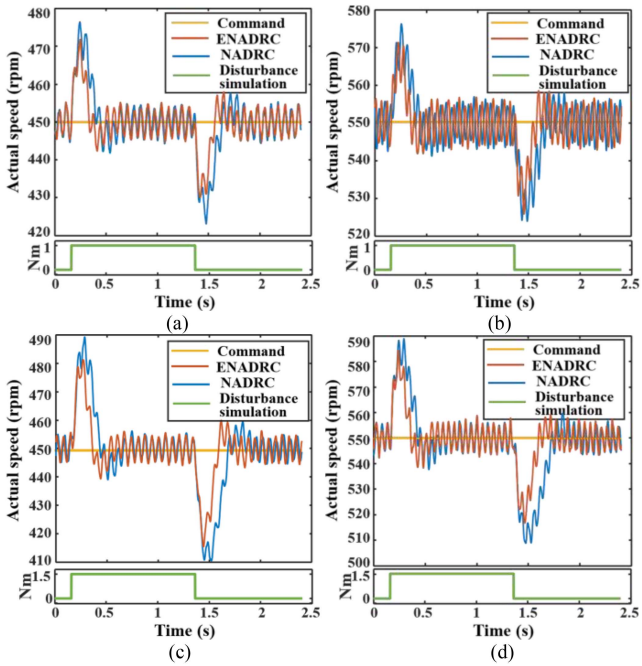

Fig. 13. Experimental curve results for different operating conditions and disturbance. (a) Comparison results of NADRC and ENADRC at 450 rpm with disturbance amplitude of 1 Nm. (b) Comparison results of NADRC and ENADRC at 550 rpm with disturbance amplitude of 1 Nm. (c) Comparison results of NADRC and ENADRC at 450 rpm with disturbance amplitude of 1.5 Nm. (d) Comparison results of NADRC and ENADRC at 550 rpm with disturbance amplitude of 1.5 Nm. (e) Comparison results of NADRC and ENADRC at 450 rpm with disturbance amplitude of 2 Nm. (f) Comparison results of NADRC and ENADRC at 500 rpm with disturbance amplitude of 2 Nm.

TABLE II
COMPARISON RESULTS FOR DIFFERENT SPEED AND DISTURBANCE

	Disturbance		$\lvert M_p \rvert$ (rpm)			t_s (s)		
	Amplitude	Process (Nm)	NADRC	ENADRC	$\triangle M$	NADRC	ENADRC	$\triangle t$
450 rpm	1 Nm	0→1	26.4	21.8	4.6	0.46	0.33	0.13
		1→0	26.8	19.5	7.3	0.46	0.32	0.14
	1.5 Nm	0→1.5	39.2	31.3	7.9	0.53	0.36	0.17
		1.5→0	39.3	34.1	5.2	0.55	0.41	0.14
	2 Nm	0→2	53.3	41.9	11.4	0.64	0.42	0.22
		2→0	58.6	44.5	14.1	0.63	0.47	0.16
550 rpm	1 Nm	0→1	26.3	21.3	5	0.47	0.37	0.1
		1→0	26.1	23	3.1	0.53	0.38	0.15
	1.5 Nm	0→1.5	38.9	34.3	4.6	0.52	0.39	0.13
		1.5→0	43.3	33.7	9.6	0.59	0.45	0.14
	2 Nm	0→2	52.1	42.9	9.2	0.58	0.41	0.17
		2→0	61	46.3	14.7	0.59	0.48	0.11

when the incoming flow is absent and the actual speed is stable, and the command is increased to reduce the actual output. The comparative experimental results are presented in Fig. 13 and Table II.

In Fig. 13(a) and (b), the simulated disturbance amplitude is set to 1 Nm. At 0.16 s, the disturbance changes from 0 to 1 Nm, and after holding the disturbance of 1 Nm for 1.2 s, it is reduced to zero at 1.36 s. Finally, this zero value is kept for 1.2 s. The maximum overshoot (M_p) and adjustment time (t_s) of ENADRC algorithm at the speeds of 450 and 550 rpm are less than those of NADRC algorithm. Similarly, the disturbance amplitude is set to 1.5 Nm in Fig. 13(c) and (d) and 2 Nm in Fig. 13(e) and (f). Considering Fig. 13(e) as an example, after disturbance of NADRC algorithm, its feedback speed deviates greatly from the command speed. The maximum overshoot speed is about 503.3 rpm when the disturbance increases at 0.16 s (about 491.9 rpm for the ENADRC algorithm), while the maximum overshoot speed is about 391.4 rpm when the disturbance decreases at 1.36 s (about 405.5 rpm for the ENADRC algorithm). This is due to reduction of NADRC algorithm potential in suppressing disturbance with the increase of disturbance amplitude. Because of introduction of λz_{22}, the ability of ENADRC in reduction of disturbance is increased, so the maximum overshoot speed and adjustment time are significantly better than NADRC. Table II shows the comparison of NADRC and ENADRC under different operating conditions. $\triangle M$ and $\triangle t$ represent the difference between NADRC and ENADRC algorithms. This difference is larger, the disturbance suppression effect of ENADRC is better. On the whole, the overshoot speed of ENADRC is obviously smaller than that of NADRC, and this advantage becomes more and more significant with the increase of disturbance amplitude. Compared with NADRC, the adjustment time of ENADRC is basically reduced by more than 0.1 s.

VI. CONCLUSION

In order to improve the dynamic response and antidisturbance capabilities of electric propulsion system equipped with propeller load, an ENADRC control method was proposed in this article. This method applied LESO to preliminarily estimate the total system disturbance, and then introduced it into ENESO. The system involved good speed response and disturbance suppression ability using the designed weight rule function. The experimental verification was carried out on the system platform, and the following conclusions are obtained:

- The proposed ENADRC control algorithm resulted in obvious advantages in the response speed of step command. Variation of weight function rules enhanced the speed response-ability.
- Based on the simulation of disturbance with different amplitudes, it was observed that the speed controller of NADRC was significantly affected by the disturbance changes.
- The ENADRC algorithm was better than NADRC in terms of disturbance suppression, especially in operating conditions with abrupt disturbance changes. This advantage is significant with the increase of disturbance amplitude.

REFERENCES

[1] P. F. Pelz, P. Leise, and M. Meck, "Sustainable aircraft design—A review on optimization methods for electric propulsion with derived optimal number of propulsors," *Prog. Aerosp. Sci.*, vol. 123, Jun. 2021, Art. no. 100714.
[2] D. Ma, L. Zhang, M. Yang, X. Xia, and S. Wang, "Review of key technologies of ultra-long-endurance solar powered unmanned aerial vehicle," *Acta Aeronautica et Astronautica Sinica*, vol. 41, 2020, Art. no. 623418.
[3] C. Zhang, C. Zhang, L. Li, and Q. Guo, "Parameter analysis of power system for solar-powered unmanned aerial vehicle," *Appl. Energy*, vol. 295, 2021, Art. no. 117031.
[4] S. Fang, Y. Wang, W. Wang, Y. Chen, and Y. Chen, "Design of permanent magnet synchronous motor servo system based on improved particle swarm optimization," *IEEE Trans. Power Electron.*, vol. 37, no. 5, pp. 5833–5846, May 2022.

[5] J. Yang, M. Dou, G. Luo, and D. Zhao, "A reset particle swarm optimization PID control of permanent magnet BLDC motor for airscrew load," *J. Northwestern Polytechnical Univ.*, vol. 34, no. 3, pp. 313–320, Apr. 2016.
[6] J. Pongfai, X. Su, H. Zhang, and W. Assawinchaichote, "PID controller autotuning design by a deterministic Q-SLP algorithm," *IEEE Access*, vol. 8, pp. 50010–50021, 2020.
[7] A. K. Junejo, W. Xu, C. Mu, M. M. Ismail, and Y. Liu, "Adaptive speed control of PMSM drive system based a new sliding-mode reaching law," *IEEE Trans. Power Electron.*, vol. 35, no. 11, pp. 12110–12121, Nov. 2020.
[8] X. Zhang, L. Sun, K. Zhao, and L. Sun, "Nonlinear speed control for PMSM system using sliding-mode control and disturbance compensation techniques," *IEEE Trans. Power Electron.*, vol. 28, no. 3, pp. 1358–1365, Mar. 2013.
[9] J. Linares-Flore, C. García-Rodríguez, H. Sira-Ramírez, and O. D. Ramírez-Cárdenas, "Robust backstepping tracking controller for low-speed PMSM positioning system: Design, analysis, and implementation," *IEEE Trans. Ind. Inf.*, vol. 11, no. 5, pp. 1130–1141, Oct. 2015.
[10] S. Li and H. Gu, "Fuzzy adaptive internal model control schemes for PMSM speed-regulation system," *IEEE Trans. Ind. Inf.*, vol. 8, no. 4, pp. 767–779, Nov. 2012.
[11] Z. Ping, T. Wang, Y. Huang, H. Wang, J. G. Lu, and Y. Li, "Internal model control of PMSM position servo system: Theory and experimental results," *IEEE Trans. Ind. Inf.*, vol. 16, no. 4, pp. 2202–2211, Apr. 2020.
[12] H. Sira-Ramirez and M. A. Oliver-Salazar, "On the robust control of buck-converter DC-motor combinations," *IEEE Trans. Power Electron.*, vol. 28, no. 8, pp. 3912–3922, Aug. 2013.
[13] Y. Zuo, X. Zhu, L. Quan, C. Zhang, Y. Du, and Z. Xiang, "Active disturbance rejection controller for speed control of electrical drives using phase-locking loop observer," *IEEE Trans. Ind. Electron.*, vol. 66, no. 3, pp. 1748–1759, Mar. 2019.
[14] B. Sun, H. Wang, T. Su, C. Sheng, and X. Lv, "Nonlinear active disturbance rejection controller design and tuning for permanent magnet synchronous motor speed control system," *Proc. CSEE*, vol. 40, no. 20, pp. 6715–6725, Oct. 2020.
[15] Z. Chen and Q. Gao, "Linear/nonlinear switching extended state observer," *Control Theory Appl.*, vol. 36, no. 6, pp. 902–908, Jun. 2019.
[16] Z. Yang, J. Jia, X. Sun, and T. Xu, "An enhanced linear ADRC strategy for a bearingless induction motor," *IEEE Trans. Transp. Electrific.*, vol. 8, no. 1, pp. 1255–1266, Mar. 2022.
[17] G. Wang, R. Liu, N. Zhao, D. Ding, and D. Xu, "Enhanced linear ADRC strategy for HF pulse voltage signal injection-based sensorless IPMSM drives," *IEEE Trans. Power Electron.*, vol. 34, no. 1, pp. 514–525, Jan. 2019.
[18] Z. Hao et al., "Linear/nonlinear active disturbance rejection switching control for permanent magnet synchronous motors," *IEEE Trans. Power Electron.*, vol. 36, no. 8, pp. 9334–9347, Aug. 2021.
[19] F. Bauer, C. M. Hackl, K. M. Smedley, and R. M. Kennel, "Multicopter with series connected propeller drives," *IEEE Trans. Control Syst. Technol.*, vol. 26, no. 2, pp. 563–574, Mar. 2018.
[20] D. Wu and K. Chen, "Frequency-domain analysis of nonlinear active disturbance rejection control via the describing function method," *IEEE Trans. Ind. Electron.*, vol. 60, no. 9, pp. 3906–3914, Sep. 2013.
[21] C. Zhang, C. Zhang, L. Li, H. Liu, and P. Fu, "Research on linear/nonlinear active disturbance rejection hybrid control method for electric propulsion system based on propeller load," *Proc. Chin. Soc. Elect. Eng.*," 2022.
[22] D. Wu and K. Chen, "Limit cycle analysis of active disturbance rejection control system with two nonlinearities," *ISA Trans.*, vol. 53, no. 4, pp. 947–954, Mar. 2014.
[23] L. Zhu et al., "Nonlinear active disturbance rejection control strategy for permanent magnet synchronous motor drives," *IEEE Trans. Energy Convers.*, vol. 37, no. 3, pp. 2119–2129, Sep. 2022.
[24] R. Yang, L.-Y. Li, M.-Y. Wang, C.-M. Zhang, and Y.-M. Zenggu, "Force ripple estimation and compensation of PMLSM with incremental extended state modeling-based Kalman filter: A practical tuning method," *IEEE Access*, vol. 7, pp. 108331–108342, 2019.
[25] F. Wang et al., "Modified active disturbance rejection control scheme with sliding mode compensation for airborne star tracker driven by permanent magnet synchronous motor," *Control Eng. Pract.*, vol. 127, Jul. 2022, Art. no. 105267.

Chaoyu Zhang received the B.S. degree in electrical engineering from East China Jiaotong University, Nanchang, China, in 2014, and the M.E. degree in electrical engineering from the Harbin Institute of Technology (HIT), Harbin, China, in 2017. He is currently working toward the Ph.D. degree with the Harbin Institute of Technology (HIT), Harbin, China.

His current research interest is mainly engaged in the research of electric propulsion system of solar-powered UAV.

Chengming Zhang received the B.E., M.E., and D.E. degrees in electrical engineering from the Harbin Institute of Technology (HIT), Harbin, China, in 2005, 2007, and 2013, respectively.

From 2013 to 2019, he was a Lecturer with the School of Electrical Engineering and Automation, HIT. Since 2019, he has been an Associate Professor with the Department of Electrical Engineering, HIT. His research areas include high efficiency motor systems, high speed motors, energy conversion and control.

Liyi Li (Senior Member, IEEE) was born in Hei Longjiang, China, in 1969. He received the B.E., M.E., and D.E. degrees from the Harbin Institute of Technology (HIT), Harbin, China, in 1991, 1995, and 2001, respectively.

Since 2004, he has been a Professor with the School of Electrical Engineering and Automation, HIT. He has authored or coauthored more than 110 technical papers, and holds 50 patents. His research areas are in control and drive of high-speed permanent magnet synchronous motors and linear motors.

Hongchen Liu (Senior Member, IEEE) received the B.S. degree in electrical engineering from Northeast Agricultural University, Harbin, China, in 2001, and the master's and Ph.D. degrees in electrical engineering from the Harbin Institute of Technology (HIT), Harbin, China, in 2003 and 2007, respectively.

In 2009, he joined the Department of Electrical Engineering, HIT, as a Lecturer, where he has been a Professor of Electrical Engineering since 2020. From 2008 to 2012, he was a Postdoctoral Fellow in Measuring and Controlling Technology and Instrument Specialty. He has authored more than 60 technical papers published in journals and conference proceedings. His current major research interests include dc–dc converter and inverter in photovoltaic system, matrix converter, and nonlinear dynamics in power electronics.